

The mode switching in pulsar J1326–6700

Z. G. WEN,^{1,2,3} W. M. YAN,^{1,3} J. P. YUAN,^{1,3} H. G. WANG,^{4,1} J. L. CHEN,⁵ M. MIJIT,⁶ R. YUEN,¹ N. WANG,^{1,3}
Z. Y. TU,¹ AND S. J. DANG^{1,7}

¹*Xinjiang Astronomical Observatory, Chinese Academy of Sciences,
150, Science-1 Street, Urumqi, Xinjiang, 830011, China*

²*Guizhou Provincial Key Laboratory of Radio Astronomy and Data Processing,
Guiyang, Guizhou, 550001, China*

³*Key laboratory of Radio Astronomy, Chinese Academy of Sciences,
Nanjing, 210008, China*

⁴*School of Physics and Electronic Engineering,
Guangzhou University, 510006, Guangzhou, PR China*

⁵*Department of Physics and Electronic Engineering,
Yuncheng University, Yuncheng, Shanxi, 044000, China*

⁶*School of Physical Science and Technology,
Xinjiang University, urumqi, Xinjiang, 830046, China*

⁷*School of Physics and Electronic Science, Guizhou Normal University,
No. 116, Baoshan Road, Yunyan Distric, Guiyang, 550001, China*

(Received XXX; Revised XXX; Accepted XXX)

Submitted to ApJ

ABSTRACT

We report on a detailed study on the mode switching in pulsar J1326–6700 by analysis the data acquired from the Parkes 64-m radio telescope at 1369 MHz. During the abnormal mode, the emission at the central and trailing components becomes extremely weak. Meanwhile, the leading emission shifts towards earlier by almost 2 degrees, and remains in this position for typically less than a minute. The mean flux density of the normal mode is almost five times that of the abnormal mode. Our data show that 85% of the time for PSR J1326–6700 was in the normal mode and 15% was in the abnormal mode. The intrinsic distributions of mode timescales can be well described by Weibull distributions, which presents a certain amount of memory in mode switching. Furthermore, a quasi-periodicity has been identified in the mode switching in pulsar J1326–6700. The estimated delay emission heights based on the kinematical effects indicate that the abnormal mode may be originated from higher altitude than the normal mode.

Keywords: stars: neutron – pulsars: general – pulsars: individual: PSR J1326–6700

1. INTRODUCTION

Pulsars are rapidly rotating, highly magnetized neutron stars which emit radio electromagnetic radiation along their magnetic axes. The discrete and regular pulses are received while our line of sight sweeps across the radio beam as the star rotates. Two primary single pulse modulations intrinsic to pulsar radio emission are

the phenomena of nulling and mode changing (or mode switching). Nulling is the abrupt cessation of pulsed emission for several periods. Mode changing is the sudden switches between two or more distinct emission patterns. Both of these effects have been investigated extensively and are suggested to be originated from large scale and persistent changes in the magnetospheric current distribution (Wang et al. 2007).

Radio strong pulsar J1326–6700 is characterized by the intriguing combination of three canonical pulse modulation phenomena: nulling, mode changing and occasional subpulse drifting (Wang et al. 2007). PSR

J1326–6700 first attracted our attention because the average pulse profiles for two modes present extremely distinct difference. During the abnormal mode episode, sporadic emission appears at the leading edge of the profile lasting for a dozen or more pulses. Meanwhile, the emission from the usual window ceases. The effect bears some resemblance to the anomalous emission events (recently referred as ‘swooshes’) presented in pulsars B1859+07 and B0919+06 (Rankin et al. 2006), whose emission shifts to an earlier longitude gradually. The possibility of conventional mode changing was ruled out because of the gradual onsets and relaxations of the events. Among several proposed explanations, the changes in emission altitude appears possible to explain the gradual nature of the event onsets and returns. However, the displacement of the emitting region requires too large vertical height in the magnetosphere which greatly exceed the height above the neutron star’s surface.

In this paper, by using the archived data observed with the Parkes 64-m radio telescope at 1369 MHz, we focus on the specific characteristics of normal and abnormal emission modes. Furthermore, a perplexing periodicity is shown in the mode switching, which may in turn open up a new potential avenue of interpretation. Details of the observations are described in Section 2. Results are presented in Section 3. The implication of our results to the emission geometry and possible mechanisms for the mode switching are discussed in Section 4. Finally, Section 5 summarizes the results and discussion.

2. OBSERVATIONS

The analyses in this paper are based on five available observations from the Parkes pulsar data archive (Hobbs et al. 2011), all of which were carried out using the Parkes 64 meter radio telescope and the multi-beam receiver. The data were recorded with one of the Parkes digital filterbank systems (PDFB3/4) in incoherent mode. Full-Stokes spectra were acquired using 512 channels across a 256 MHz passband centered at 1369 MHz radio frequency. The data were integrated in time for 256 μ s per spectrum before recording to disk with 8-bit quantization. In order to calibrate flux and polarization precisely, pulsed noise signals were linearly injected into the feed horn prior to the first-stage low-noise amplifier. The system equivalent flux density (SEFD) on cold sky was determined via paired observations of the unpolarized extragalaxy 3C218 (Hydra A) with an assumed flux at 1400 MHz of 43.1 Jy. The detailed information of the observations are listed in Table 1.

The PSRCHIVE¹ (Hotan et al. 2004) and DSPSR² (van Straten & Bailes 2011) pulsar analysis software packages were used in off-line data reduction. Initially, the single pulse integrations were obtained by folding the data into 1024 phase bins per pulse period. The pulsar’s rotational ephemerides was taken from the ATNF pulsar catalogue V1.61³ (Manchester et al. 2005). The radio frequency interference (RFI) was then mitigated automatically in the frequency domain using median filtering technique and 5 per cent of each band edge were zero weighted. Subsequently, the data were calibrated to compensate for instrumental gain and phase variations across the band, converted to Stokes parameters, and placed on a flux density scale. From the resulting multi-frequency polarization profiles, the rotation measure (RM) was obtained by brute-force search for peak linear polarization and then iterative refinement of differential position angle following the method described by Han et al. (2006). The cause of significant differences in the RM value of PSR J1326–6700 from the different observations is not clear. Finally, the full-Stokes individual pulses were obtained by removing the dispersive smearing between sub-channels, which provide the basis for the analyses described in the following sections.

3. RESULTS

3.1. Pulse sequence dynamics

With the benefit of Parkes high sensitivity, PSR J1326–6700 is bright enough to study its single pulse sequences, and a color-coded pulse sequence displays several of the pulsar’s emission behaviors in the top-left panel of Figure 1. An intriguing combination of nulling and mode changing is clearly shown. The pulses with no detectable emission from central and trailing components are clearly visible. During the partial nulls, an obvious abnormal mode emission appears to flicker on at the leading edge the profile for typically less than a minute. The sporadic emission in the abnormal mode is frequently separated by short nulls. On several occasions, the two modes are separated by a complete null interval where the coherent radio emission in the whole pulse period ceases.

3.2. Pulse energy distribution

In order to characterize the pulse nulling properties statistically, the pulse energy distributions for the on-pulse region and off-pulse region with similar lengths,

¹ <https://psrchive.sourceforge.net/>

² <http://dspsr.sourceforge.net/>

³ <http://www.atnf.csiro.au/research/pulsar/psrcat/>

Table 1. Summary of radio observations of PSR J1326–6700.

Date (yyyy–mm–dd)	Start time (UTC)	Backend	SEFD (Jy)	Duration (s)	Flux density (mJy)	RM (rad m ⁻²)
2012–01–15	20:14:24	PDFB4	37.1	1505	11.26 ± 0.02	-46.6 ± 0.9
2014–05–25	03:36:17	PDFB4	35.7	7204	9.25 ± 0.01	-56.3 ± 0.7
2014–05–30	06:04:42	PDFB4	35.6	6384	10.92 ± 0.02	-52.3 ± 0.8
2014–10–15	22:07:09	PDFB3	35.3	7205	22.99 ± 0.03	-25 ± 1
2014–12–02	20:38:09	PDFB4	...	1466

Notes. No paired calibrator was observed for the 2014–12–02 observation. The paired calibrator for the 2014–10–15 observation was recorded with the PDFB4, whereas the target source was recorded with the PDFB3. Therefore, the great deviations of flux density and RM are the result of equipment difference.

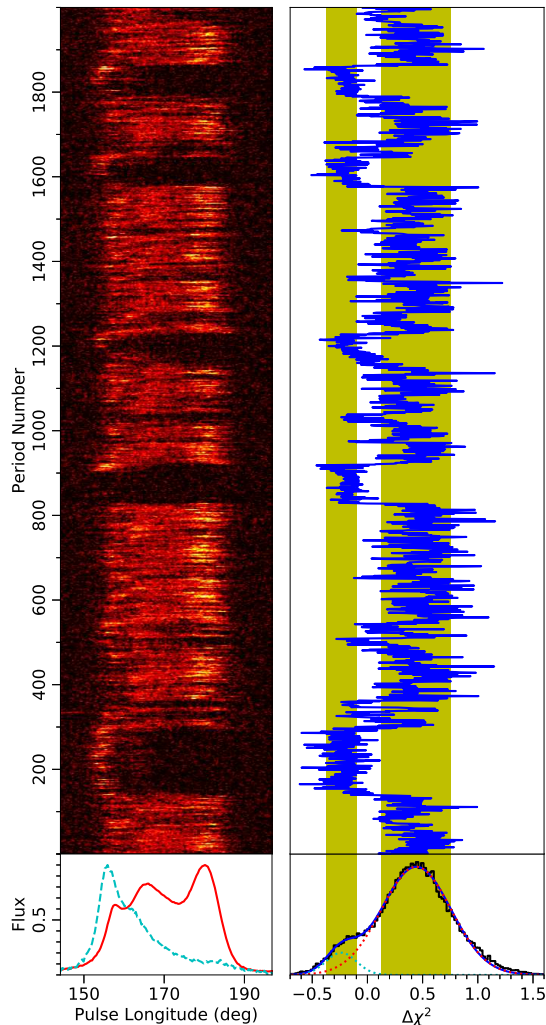


Figure 1. Top-left panel: longitude-time diagram showing intensity variations for 2000 individual pulses from PSR J1326–6700. Time extends from left to right through pulses and successive pulses are plotted from bottom to top. Bottom-left panel: the comparisons of the mean pulse profile for the normal emission mode (solid red) and abnormal emission mode (dashed cyan). Top-right panel: the $\Delta\chi^2$ for the corresponding profiles on the left. Bottom-right panel: histogram of the $\Delta\chi^2$ for the entire data set is indicated with the black solid line. The blue solid line represents the fitting based on the combination of two Gaussian components (dashed cyan and dashed red lines). The yellow bars indicate the $\pm 1\sigma$ range around the fitted two peaks.

after a normalisation by the mean pulse energy, are presented in Figure 2. The off-pulse energy histogram, centering around zeros, represents a Gaussian random noise

contributed by the telescope noise. While the on-pulse energy distribution shows the presence of two distinct regions, which corresponds to bistable emission modes. The two peaks as determined from a fit with the sum of two normal distributions are obviously larger than zero, which implies that the apparent nulls are in an abnormal emission mode rather than real null pulses.

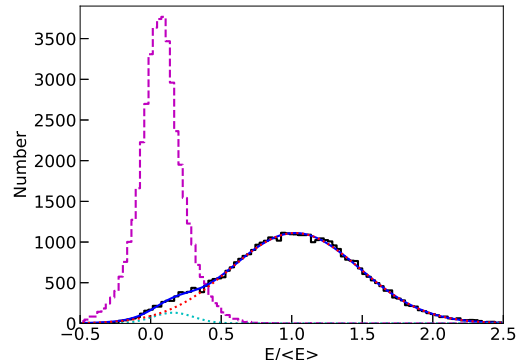


Figure 2. Pulse energy distributions for the on-pulse (black solid histogram) and off-pulse (magenta dashed histogram) regions are calculated from all observations. The energies are normalized by their respective mean on-pulse energies. The blue solid line represents the fitting for the on-pulse energy distribution based on the combination of two Gaussian components (cyan and red dotted lines) with the R-square of 0.997.

3.3. Identification of mode switching

The single pulse energy distribution indicates the existence of mode switching in PSR J1326–6700, with the pulse profile switching on timescales of seconds between two quasi-stable modes, which differ in intensity. In order to determine mode switching properties such as the timescale and polarization, a quantitative metric is defined to distinguish whether an individual pulse belongs to the normal or the abnormal emission mode, which is given by (Mahajan et al. 2018)

$$\Delta\chi_i^2 = \sum_{\phi} \frac{(p_i(\phi) - p_a(\phi))^2 - (p_i(\phi) - p_n(\phi))^2}{\sigma(\phi)^2}, \quad (1)$$

where $p_i(\phi)$ is an individual pulse profile, $p_n(\phi)$ and $p_a(\phi)$ are the average pulse profiles for normal and abnormal modes respectively, and $\sigma(\phi)$ is the standard deviation from the mean of the entire data set. The mode metric $\Delta\chi^2$ corresponding to individual pulses are indicated in the top-right panel of Figure 1.

A histogram of mode metric for our whole data set of ~ 44 thousand pulses is shown in the bottom-right panel

of Figure 1, which clearly shows a bi-modal distribution. We fit the histogram with a sum of two normal distributions, finding centers for the normal and abnormal mode of $\Delta\chi^2 = 0.442 \pm 0.003$ and -0.238 ± 0.009 , respectively, and associated widths of $\sigma_{\Delta\chi^2} = 0.315 \pm 0.004$ and 0.138 ± 0.009 . The $\Delta\chi^2$ distribution of the normal mode is considerably wider than that of the abnormal mode, which may indicate that the abnormal mode is more stable than the normal mode, and the timescale for the normal mode to get stable is longer than that for the abnormal mode.

It is noted that some contamination by mode transitions is clearly presented, and it is not always obvious to which mode an individual pulse belongs due to low signal-to-noise ratio (S/N). As suggested that the durations of transitions do not necessarily represent the true time spans for which mode changes occur, a $\Delta\chi^2$ threshold is determined as the center of the inner 1σ boundaries of normal and abnormal modes. Thus, all of the individual pulses are associated with either the normal or the abnormal mode.

The average pulse profiles for the normal and abnormal modes are shown in Figure 3, where the pulse peaks are normalized to unity. A combination of three Gaussian components is adopted to fit the observed profiles. The best-fitted parameters determined using the Levenberg-Marquardt algorithm (Press et al. 1992) are presented in Table 2 with R-square of 0.996 and 0.998 for the normal and abnormal modes, respectively. It demonstrates the existence of three emission components in the abnormal mode. The relative amplitudes of the central and trailing components decrease with respect to the leading component, and the three components shift earlier in pulse phase.

3.4. Mode fractions and timescale

In our observations, PSR J1326–6700 spends 85% of the time in the normal mode, and 15% in the abnormal mode. The probability density functions (PDFs) for the lengths of the normal and abnormal modes taken from all observations together are presented in the upper and lower panels of Figure 4, respectively. They show that the occurrence of both the modes decreases at longer timescales. The PDFs of the two modes are well fitted by a Weibull distribution:

$$P(\Delta t) = \frac{k}{\lambda} \left(\frac{\Delta t - \theta}{\lambda} \right)^{k-1} e^{-\left(\frac{\Delta t - \theta}{\lambda} \right)^k}, \quad (2)$$

where k is the shape parameter, λ is the scale parameter and θ is the location parameter. Considering the asymmetric distributions, the fittings are performed on unbinned data by maximum likelihood estimation. The best fitting coefficients are estimated to

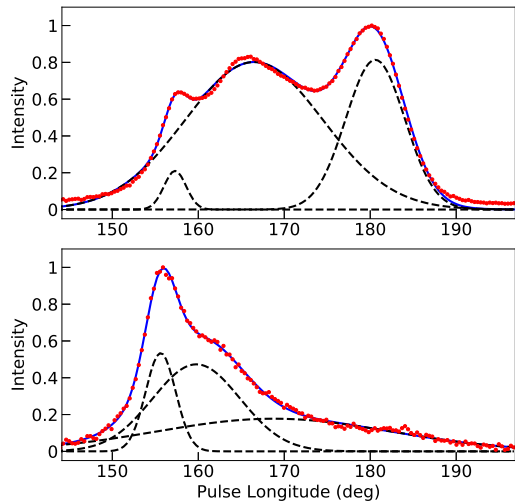


Figure 3. Observed pulse profiles (red dots) for the normal (upper) and abnormal modes emitted from PSR J1326–6700. The blue solid line represents the fitting based on the combination of three Gaussian components (black dashed lines). Here the profiles have been scaled to the same height to show the change in the pulse location and shape.

be $k = 0.79 \pm 0.03$, $\lambda = 67 \pm 4$, $\theta = 6.6 \pm 0.5$ and R-square=0.991 for the normal mode, and $k = 0.81 \pm 0.03$, $\lambda = 11.8 \pm 0.7$, $\theta = 2.81 \pm 0.04$ and R-square=0.998 for the abnormal mode. To validate the goodness-of-fit of the Weibull distribution fits, a one-sample non-parametric Anderson-Darling test is carried out. The durations of the normal and abnormal emission modes are both drawn from Weibull distributions at 75% confidence level. For both normal and abnormal modes, the Weibull distribution is applied to all observations. The same parameters are obtained at lower significance level, implying that the underlying physical processes which produce the moding are fixed and unchanging.

The Weibull distribution is commonly used to analyze life data. A $k < 1$ implies that the probability of a mode change occurring decreases with time, the shorter the pulsar is in a mode. If $k = 1$, an exponential distribution is produced, which indicates that the probability of a mode change occurring is time-invariant. If $k > 1$, the occurring of mode changing increases with time. The best fitted power-law distributions for both modes are shown in Figure 4 as well, which do not fit the observed duration distributions well. For PSR B0919+06, the abnormal emission events occur randomly about every 1000-3000 periods (Han et al. 2016), which is much longer than PSR J1326–6700.

Table 2. Parameters of the fitted Gaussian profile components for both emission modes from PSR J1326–6700, I_i is the amplitude of the i th Gaussian component, ϕ_i is the peak longitude and W_i is the full width at half peak.

Mode	I_1	ϕ_1 (deg)	W_1 (deg)	I_2	ϕ_2 (deg)	W_2 (deg)	I_3	ϕ_3 (deg)	W_3 (deg)
Normal	0.21 ± 0.01	157.30 ± 0.07	2.6 ± 0.1	0.802 ± 0.004	166.5 ± 0.1	16.0 ± 0.1	0.81 ± 0.01	180.59 ± 0.04	6.87 ± 0.06
Abnormal	0.53 ± 0.01	155.62 ± 0.03	3.50 ± 0.05	0.47 ± 0.01	159.8 ± 0.1	10.2 ± 0.1	0.177 ± 0.005	168.8 ± 0.5	27.4 ± 0.4

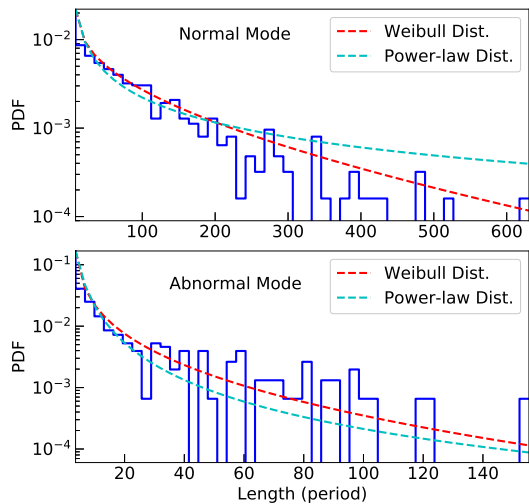


Figure 4. Duration distributions for the normal (top panel) and abnormal (bottom panel) modes taken from all observations together. The best-fit Weibull and power-law distributions for each mode are overdrawn.

3.5. Mode-segregated polarimetric profiles

In order to understand the emission properties further, sets of normal and abnormal integrated polarimetric profiles are constructed from 2012–01–15, 2014–05–25 and 2014–05–30 observations, and shown in Figure 5. The bottom panels present the total intensity (black solid curves), total linear polarization (red dashed lines) and circular polarization (blue dotted lines). The upper panels give the linear polarized position angle (hereafter PA) histograms for all single pulses, as well as the average PA traverses for normal and abnormal modes. To limit the effects of measurement uncertainties, the PAs for each single pulse are estimated at longitudes where the linear polarization power is more than 6 times the noise rms in the off pulse region.

The asymmetric total power profile of the normal mode has three main emission components, with the trailing one the strongest. During the abnormal emission state, however, the mean pulse profile is very different in amplitude and pulse phase. The emission from the normal profile ceases and the abnormal emission emerges at a new leading component. The abnormal profile possesses a single emission component with sharp leading and gradual trailing edges, and the profile position shifts markedly earlier. The mean flux density of normal mode is around 4 times brighter than that of abnormal mode. Table 3 lists the mean flux density, W_{50} (width of pulse at 50% of peak) and W_{10} (width of pulse at 10% of peak) of both normal and abnormal modes. Note that

the strong linear polarization under the trailing feature simply disappears during the abnormal mode. Significant right-circular polarization is observed in the center of the normal profile. The abnormal mode shows a marginal circular polarization over the whole profile.

The PA exhibits a fast swing across the profile, and a ‘S’-shaped sweep is presented, which may indicate that we are seeing the whole conal beam. Then the line of sight geometry can be assessed by fitting the rotating vector model (RVM, Radhakrishnan & Cooke 1969) to the PA traverse. It is noted that for both emission modes a jump of around of 60° is shown in the PA under the leading component which is also associated with a substantial dip in the linear polarization. For the normal mode, a bimodal distribution of PAs separated by around of 80° predominates in the trailing emission region as well. The two preferred PAs at the leading and trailing components manifest the presence of two orthogonal polarization states. The classical RVM curve could be severely corrupted by the variations in strength between the two modes. In order to refrain the modal effects, only the pulse longitudes where the average PA traverse is in good agreement with the single pulse PA in the central component are considered. The best fits to the RVM are shown as red curves in the upper panels of Figure 5. The viewing geometries for normal and abnormal modes are specified with the values of magnetic inclination angle (α), impact angle (β), position angle offset (ψ_0) and fiducial plane angle (ϕ_0), which are listed in Table 3. As shown that the quantities of ϕ_0 and ψ_0 are significantly constrained. However, the α and β values obtained from these fits are extremely covariant and unreliable due to the limited duty cycle of the profile (Mitra & Li 2004). For instance, Figure 6 shows the reduced χ^2 values of the fit as a function of α and β for the normal mode. Here, the best fit occurs where χ^2 reaches a minimum. Evidently, there are a number of combinations of α and β which provide equally acceptable fits. Therefore, the actual geometry of the system can not be necessarily represented by the derived angles. From the RVM fit alone, we can conclude that $0^\circ < \beta < 10^\circ$, corresponding to a positive gradient of the PA swing. Nevertheless, the fact that α is practically unconstrained. More constraints on these parameters are described in the discussion section.

3.6. Fluctuation spectra

As shown in Figure 1, the mode switching events seem to appear such frequently with a rough regularity of several hundred pulses in PSR J1326–6700. The longitude-resolved fluctuation spectra (LRFS; Backer 1973) are calculated to investigate whether the mode

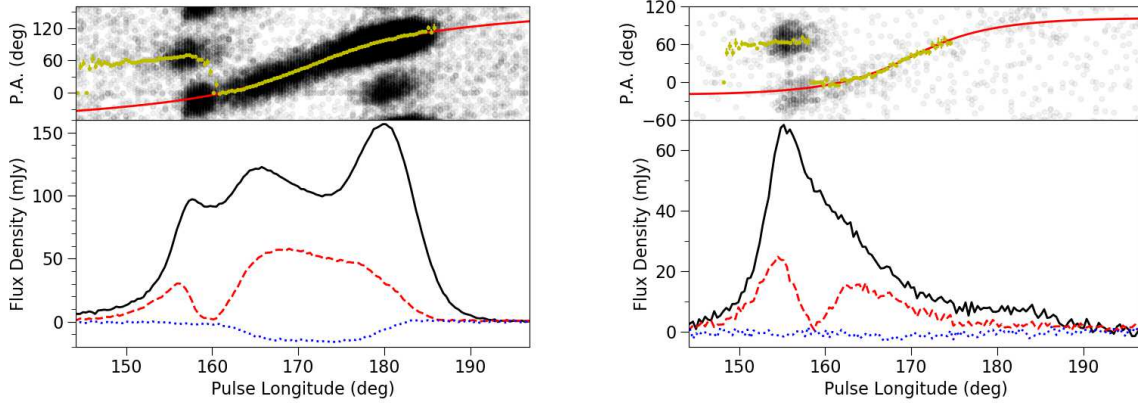


Figure 5. The averaged polarization profiles of normal (left) and abnormal (right) modes for PSR J1326–6700 at 1369 MHz. The lower panel gives the total intensity (Stokes I, black solid curve), the total linear (Stokes $L = \sqrt{Q^2 + U^2}$, red dashed curve), and the circular polarization (Stokes V, blue dash-dotted curve). The upper panel presents the longitude-dependent histogram of measured position angle $\psi = \frac{1}{2}\tan^{-1}(U/Q)$ along with the position angle of the mean profile, a fitted curve computed based on the rotating vector model is shown in the red curve.

Table 3. List of the parameters during the normal and abnormal modes of PSR J1326–6700. The angles α , β , ϕ_0 and ψ_0 are fits obtained from the RVM.

Mode	% of pulses	Flux density (mJy)	W_{50} (deg)	W_{10} (deg)	α (deg)	β (deg)	ϕ_0 (deg)	ψ_0 (deg)
Normal	85%	11.40 ± 0.01	27.9 ± 0.2	37.0 ± 0.5	179.5 ± 4926.0	0.08 ± 782.45	171.3 ± 0.2	50.5 ± 0.9
Abnormal	15%	2.44 ± 0.01	10.4 ± 0.3	37.3 ± 0.7	0.07 ± 35866.97	0.01 ± 5523.61	170.1 ± 0.6	41 ± 3

Notes. The extremely high uncertainties in α and β reflect their covariant relationship.

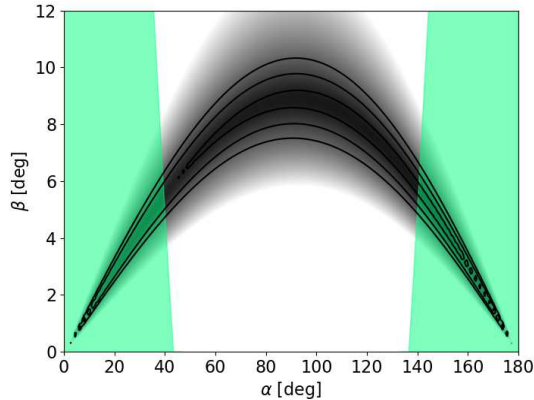


Figure 6. The results of fitting an RVM curve for each (α, β) combination for normal mode. The reduced chi-square (χ^2) of the fit is shown as the gray scale, with the darkest value corresponding to the best fit. Evidently, α and β are highly correlated resulting in an ambiguity in the determination of α . The black contour lines represent $1-\sigma$, $2-\sigma$ and $3-\sigma$ confidence boundaries. The green regions show constrained viewing geometries allowed by the observed pulse width.

switching occurs with a regularity. This involves performing discrete fast Fourier transforms along each longitude bin within the pulse window. Any periodicity will be indicated as a peak in the Fourier spectrum. The spectrum of the 2014-10-15 observation of PSR J1326–6700, shown in the top panel of Figure 7, remarkably displays a well-defined periodic feature with a peak frequency at $0.004 \text{ cycles period}^{-1}$ associated most strongly with the central and trailing components of the profile. The latter property ties this principal fluctuation to the mode switching events, since a longitudinal shift of emission would be most evident at these longitudes. A more accurate value for the total fluctuation frequency can be determined with the peak value with an uncertainty estimated as $\text{FWHM}/2\sqrt{2\ln(2)}$, where FWHM is the full width at half-maximum of the peak feature and $2\sqrt{2\ln(2)}$ is the scaling for Gaussian approximation (Basu et al. 2019), giving $P_f = 256 \pm 30$ rotation periods. The total fluctuation spectra of all observations are shown in the following lower panels of Figure 7. The somewhat long 2014-05-25 and 2014-05-30 spectra present period of 205 ± 18 and 341 ± 48 , respectively. The short 2014-12-02 observation shows a strong feature at $0.0059 \text{ cycles period}^{-1}$ with a period of 171 ± 20 stellar rotations. Three strong peaks at 113, 147, and 333 periods are shown in the 2012-01-15 spectrum. The somewhat different spectra presented maybe caused by the wide spreading of fluctuation power in these observations. Similar periodicities have also been

identified in PSR B0919+06 with an approximate period of 150 rotation periods and PSR B1859+07 with a rough period of 700 rotations (Wahl et al. 2016). The quasi-periodicity found in the five separate fluctuation spectra is time variant, it is consequence of taking five separate observational samples of unchanging Weibull distributions for the normal and abnormal modes.

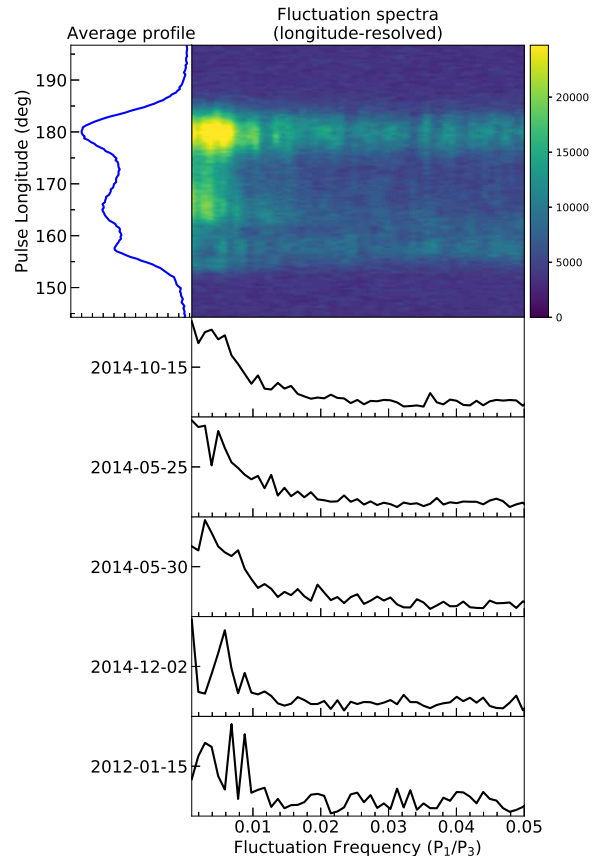


Figure 7. Fluctuation spectra of PSR J1326–6700, showing evidence for mode switching periodicity. The longitude-resolved fluctuation spectrum for 2014-10-15 is shown in the top right panel. The averaged pulse profile is shown in the left panel, and the lower panel displays the overall fluctuation spectrum. The following lower panels display the overall fluctuation spectra for 2014-05-25, 2014-05-30, 2014-12-02 and 2012-01-15, respectively. Fourier transforms of length 1024 were used. Note that all of the overall fluctuation spectra are plotted only to $0.05 \text{ cycles period}^{-1}$. The feature at $0.0039 \text{ cycles period}^{-1}$ corresponds to a periodicity of 256 rotation periods.

In order to determine whether the periodic modulations are originated from occasional phase drifting as suggested by Wang et al. (2007), the two-dimensional fluctuation spectra (2DFS; Edwards & Stappers 2002)

are calculated. No evidence of drifting subpulses is shown in our observations.

4. DISCUSSION

4.1. The viewing geometry

The location of the radio emission region in pulsar magnetosphere remains a major uncertainty in our understanding of pulsar emission physics. The emission altitude calculated using a geometrical approach involves a dipole field configuration where the viewing geometry has to be specified (Phillips 1992). However, α and β values cannot be unambiguously determined from the RVM fitting as shown in Figure 6. An independent procedure with significant advantages for estimating emission heights has been developed by (Blaskiewicz et al. 1991). The steepest gradient point of the PA traverse is expected to have a time lag with respect to the centroid of the total intensity profile due to relativistic effects such as aberration and retardation. Then the absolute emission height at the frequency of observation can be converted from this time delay ($\Delta\phi$), and is given by

$$h_{\text{em}} = \frac{Pc\Delta\phi}{8\pi}, \quad (3)$$

where P is the rotation period of the star and c is the speed of light. The profile centroid ϕ_1 is identified with the pulse longitude midway between the outermost edges of the pulse intensity profile. The uncertainty in ϕ_1 is estimated by $\sigma(\phi_1) = 2\sigma(I)/|dI/d\phi|$, where $\sigma(I)$ represents the noise level, and $dI/d\phi$ is the gradient of the profile in the vicinity of the edge. The pulse longitude at which the steepest slope of the PA curve occurs can be measured at the fiducial plane. The derived emission heights for normal and abnormal modes are given in Table 4.

Table 4. Profile centroid, beam width, W_{open} and emission altitude estimates for normal and abnormal modes.

Mode	ϕ_1 (deg)	r_{em} (km)	ρ (deg)	W_{open} (deg)
Normal	167.9±0.5	380±61	10.6±0.8	46.0±0.5
Abnormal	161.1±1.4	1012±172	17.2±1.5	46.0±0.7

Subsequently, the half opening angle of the radio emission beam can be determined from the emission height under the assumption that the beam is bounded by tangents to the last open field lines of a dipolar magnetic field. The half opening angle is obtained using the formula

$$\rho = \theta_{\text{PC}} + \arctan\left(\frac{1}{2}\tan\theta_{\text{PC}}\right), \quad (4)$$

where θ_{PC} denotes the angular radius of the open field line region, and is given by

$$\theta_{\text{PC}} = \arcsin\left(\sqrt{\frac{2\pi h_{\text{em}}}{Pc}}\right) \quad (5)$$

(Lyne & Graham-Smith 2012).

As a result, the values of α and β can be constrained from

$$\cos\rho = \cos\alpha\cos(\alpha + \beta) + \sin\alpha\sin(\alpha + \beta)\cos\left(\frac{W_{\text{open}}}{2}\right) \quad (6)$$

(Gil et al. 1984), where W_{open} is the range of rotational longitude for which the line of sight samples the open field line region. W_{open} is taken to be twice the difference in phase between the fiducial plane position and the pulse edge furthest from it (Rookyard et al. 2015). The green areas shown in Figure 6 show the favoured viewing geometry that can produce a pulse of the measured width. The magnetic axis is relatively aligned with the pulsar's rotation axis with $\alpha < 45^\circ$.

4.2. Probing the mode switching mechanism

As shown in Figure 1, the time-dependent mode changing presents gradual earlier shift pattern of the emission longitude, and occasional nulls interrupt the abnormal emission state. The W_{10} remains constant for both emission modes. However, the W_{50} during the abnormal mode narrows (see Table 3). Furthermore, in PSR J1326–6700 the profile changes occur quasi-periodically, implying the existence of a different rotation frequency from that of the star. It is suggested that the magnetosphere does not corotate with the star, and the structure of the magnetosphere changes in a quasi-periodic pattern. For instance, recently, the swooshes were identified with a quasi-periodicity in pulsar B1859+07 and possibly B0919+06 (Wahl et al. 2016).

The origin of mode changing has been remaining a mystery since the first discovery of mode switching in PSR B1237+25 (Backer 1970). There is increasing evidence that the mode changing is possibly caused by changes of magnetospheric particle current flow (Lyne et al. 1971). Nevertheless, the underlying physical mechanism for the change of magnetosphere state is not clear yet. Lyne et al. (2010) presented the correlated changes in the pulse profile and in the timing noise for six pulsars. The switching between the radio-quiet ‘off’ and radio-loud ‘on’ states in the intermittent pulsar B1931+24 was found to be correlated with the slowing down rate of the pulsar Kramer et al. (2006). The abrupt changes of emission mode is suggested that the pulsar jumps between two different magnetospheric states, and a causal connection between the

radio emission and the torque on the star is established physically. A purely magnetospheric model for observed abrupt changes in pulsar radio profile is applied to the swooshing in PSR B0919+06 (Yuen & Melrose 2017). Therefore, the phase shift during the abnormal emission mode in PSR J1326–6700 can be described by the shifts in the intersection points of the trajectory with the emission spot as well. A long term monitoring is suggested to investigate whether the spin-down rate correlates with the shifting between the two profile states.

The delay emission heights for both modes derived using the relativistic beaming model based on effects of aberration and retardation are given in Table 4. It is found that the abnormal emission arises at higher altitude from the surface of the neutron star while the normal mode arise closer to the stellar surface, corresponding to a jump from 0.015 to 0.04 light cylinder radius. Furthermore, the beam opening angle of the abnormal mode is wider than that of the normal mode. A possible model is constructed, wherein the emission of both modes comes from the same magnetic flux surface, but from different heights at a fixed frequency (van Leeuwen et al. 2003). As shown in Figure 8, the altitude at a fixed frequency increases when the emission changes from normal mode to abnormal mode. According to the traditional vacuum gap model (Ruderman & Sutherland 1975), the transition from normal mode to abnormal mode occurs by an increase in height of the voltage gap. As a result the altitude of emission increases.

Alternative possible origins of the anomalous variations in the on-pulse phase have been proposed. Rankin et al. (2006) suggested that the swooshes could be caused by ‘partial conal’ emission, where the emission region was partly obscured. The binary companions in the light cylinder orbits was adopted to interpret the inter-swoosh quasi-period (Wahl et al. 2016).

5. CONCLUSIONS

PSR J1326–6700 presents two emission modes based on the distribution of $\Delta\chi^2$ in our work. Usually, the emission comes from three regions of the profile, but occasionally the emission weakens at the central and trailing components along with shifts of the leading emission towards earlier to illuminate the leading edge of the profile for less than a minute. The overall intensity of the normal mode is almost five times that of the abnormal mode. The $\Delta\chi^2$ distribution of the normal mode is wider than that of the abnormal mode, which suggests that the normal emission mode is less stable than the abnormal mode. The pulsar spent 85% of the total observation time in the normal mode, and 15% in

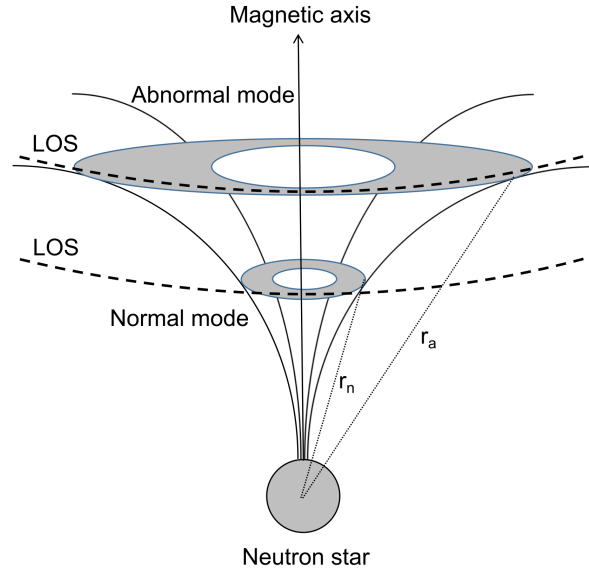


Figure 8. Schematic diagram explaining the observed behavior of two emission modes of PSR J1326–6700. The normal and abnormal emission regions, symmetrical around the magnetic axis, are assumed to be generated at different altitudes, r_n and r_a , respectively. The beam size expands during the abnormal emission state, as shown by the trajectories of line of sight (LOS).

the abnormal mode. The durations of both emission modes can be well described by Weibull distributions with shape parameters less than 1, which indicates that the occurrence of mode changing is clustered. Furthermore, a quasi-periodicity was found in the mode switching in pulsar J1326–6700.

The high S/N profiles have allowed us to estimate the magnetospheric height of the 1369 MHz emission, based on the delay-radius relation and the lag between the phase at the steepest PA gradient and that at the profile’s mid-point. Using the observed phase lags, the emission height of the abnormal mode is estimated to be around three times higher than that of the normal mode. It is evident that the simultaneous multi-wavelength polarization observations are necessary to offer further insights into the frequency evolution of mode changing in PSR J1326–6700 and to gain a full description of the physical processes driving the changes. For instance, why such a emission altitude change should occur and why the height should increase rather than decrease during the abnormal mode.

ACKNOWLEDGEMENTS

We are grateful the referee for helpful comments. Much of this work was made possible by grant support from the Chinese National Science Foundation Grant (U1838109, U1731238, U1831102, U1631106,

11873080), the West Light Foundation of Chinese Academy of Sciences (WLF 2016-QNXZ-B-24), and the National Basic Research Program of China (973 Program 2015CB857100). J.P.Y. is supported by a prospective project of the Astronomical Research Center of the Chinese Academy of Sciences. N.W. is supported by the National Program on Key Research and Development Project (grant No. 2016YFA0400804). H.G.W. is supported by the 2018 project of Xinjiang uygur autonomous region of China for flexibly fetching in upscale

talents. J.L.C. is supported by the Scientific and Technological Innovation Programs of Higher Education Institutions in Shanxi (grant No. 2019L0863). The project was supported by Open Fund of Guizhou Provincial Key Laboratory of Radio Astronomy and Data Processing. We thank members of the Pulsar Group at XAO for helpful discussions. The Parkes radio telescope is part of the Australia Telescope National Facility, which is funded by the Australian Government for operation as a National Facility managed by CSIRO.

REFERENCES

- Backer, D. C. 1970, *Nature*, 228, 1297, doi: [10.1038/2281297a0](https://doi.org/10.1038/2281297a0)
- . 1973, *ApJ*, 182, 245, doi: [10.1086/152134](https://doi.org/10.1086/152134)
- Basu, R., Paul, A., & Mitra, D. 2019, *MNRAS*, 486, 5216, doi: [10.1093/mnras/stz1225](https://doi.org/10.1093/mnras/stz1225)
- Blaskiewicz, M., Cordes, J. M., & Wasserman, I. 1991, *ApJ*, 370, 643, doi: [10.1086/169850](https://doi.org/10.1086/169850)
- Edwards, R. T., & Stappers, B. W. 2002, *A&A*, 393, 733, doi: [10.1051/0004-6361:20021067](https://doi.org/10.1051/0004-6361:20021067)
- Gil, J., Gronkowski, P., & Rudnicki, W. 1984, *A&A*, 132, 312
- Han, J., Han, J. L., Peng, L.-X., et al. 2016, *MNRAS*, 456, 3413, doi: [10.1093/mnras/stv2891](https://doi.org/10.1093/mnras/stv2891)
- Han, J. L., Manchester, R. N., Lyne, A. G., Qiao, G. J., & van Straten, W. 2006, *ApJ*, 642, 868, doi: [10.1086/501444](https://doi.org/10.1086/501444)
- Hobbs, G., Miller, D., Manchester, R. N., et al. 2011, *PASA*, 28, 202, doi: [10.1071/AS11016](https://doi.org/10.1071/AS11016)
- Hotan, A. W., van Straten, W., & Manchester, R. N. 2004, *PASA*, 21, 302, doi: [10.1071/AS04022](https://doi.org/10.1071/AS04022)
- Kramer, M., Lyne, A. G., O'Brien, J. T., Jordan, C. A., & Lorimer, D. R. 2006, *Science*, 312, 549, doi: [10.1126/science.1124060](https://doi.org/10.1126/science.1124060)
- Lyne, A., & Graham-Smith, F. 2012, *Pulsar Astronomy*
- Lyne, A., Hobbs, G., Kramer, M., Stairs, I., & Stappers, B. 2010, *Science*, 329, 408, doi: [10.1126/science.1186683](https://doi.org/10.1126/science.1186683)
- Lyne, A. G., Smith, F. G., & Graham, D. A. 1971, *MNRAS*, 153, 337, doi: [10.1093/mnras/153.3.337](https://doi.org/10.1093/mnras/153.3.337)
- Mahajan, N., van Kerkwijk, M. H., Main, R., & Pen, U.-L. 2018, *ApJL*, 867, L2, doi: [10.3847/2041-8213/aae713](https://doi.org/10.3847/2041-8213/aae713)
- Manchester, R. N., Hobbs, G. B., Teoh, A., & Hobbs, M. 2005, *AJ*, 129, 1993, doi: [10.1086/428488](https://doi.org/10.1086/428488)
- Mitra, D., & Li, X. H. 2004, *A&A*, 421, 215, doi: [10.1051/0004-6361:20034094](https://doi.org/10.1051/0004-6361:20034094)
- Phillips, J. A. 1992, *ApJ*, 385, 282, doi: [10.1086/170936](https://doi.org/10.1086/170936)
- Press, W. H., Teukolsky, S. A., Vetterling, W. T., & Flannery, B. P. 1992, *Numerical recipes in C. The art of scientific computing*
- Radhakrishnan, V., & Cooke, D. J. 1969, *Astrophys. Lett.*, 3, 225
- Rankin, J. M., Rodriguez, C., & Wright, G. A. E. 2006, *MNRAS*, 370, 673, doi: [10.1111/j.1365-2966.2006.10512.x](https://doi.org/10.1111/j.1365-2966.2006.10512.x)
- Rookyard, S. C., Weltevrede, P., & Johnston, S. 2015, *MNRAS*, 446, 3356, doi: [10.1093/mnras/stu2083](https://doi.org/10.1093/mnras/stu2083)
- Ruderman, M. A., & Sutherland, P. G. 1975, *ApJ*, 196, 51, doi: [10.1086/153393](https://doi.org/10.1086/153393)
- van Leeuwen, A. G. J., Stappers, B. W., Ramachandran, R., & Rankin, J. M. 2003, *A&A*, 399, 223, doi: [10.1051/0004-6361:20021630](https://doi.org/10.1051/0004-6361:20021630)
- van Straten, W., & Bailes, M. 2011, *PASA*, 28, 1, doi: [10.1071/AS10021](https://doi.org/10.1071/AS10021)
- Wahl, H. M., Orfeo, D. J., Rankin, J. M., & Weisberg, J. M. 2016, *MNRAS*, 461, 3740, doi: [10.1093/mnras/stw1589](https://doi.org/10.1093/mnras/stw1589)
- Wang, N., Manchester, R. N., & Johnston, S. 2007, *MNRAS*, 377, 1383, doi: [10.1111/j.1365-2966.2007.11703.x](https://doi.org/10.1111/j.1365-2966.2007.11703.x)
- Yuen, R., & Melrose, D. B. 2017, *MNRAS*, 469, 2049, doi: [10.1093/mnras/stx1023](https://doi.org/10.1093/mnras/stx1023)